15TH IEA HEAT PUMP CONFERENCE
MAY 26–29, 2026 | HOFBURG
VIENNA 2026
DECARBONISATION THROUGH INNOVATION

Development of a cascaded R-717 / R-601 heat pump for heat supply above 160 °C – integration of industrial waste heat

Hannes Trumpf[a*], Ole Fredrich[b], Yixia Xu[a], Christiane Thomas[a]

[a]*Technische Universität Dresden,*
Schaufler Chair of Refrigeration, Cryogenics and Compressor Technology,
01062 Dresden, Germany,
[b]*GEA Refrigeration Germany GmbH,*
13509 Berlin, Germany

Abstract

High-temperature heat pumps are a key technology for the defossilization of industrial processes. The decision to deploy a heat pump is primarily dependent on the required temperature lift, which significantly influences the coefficient of performance (COP) of the system. With the increasing need for efficient solutions, advanced heat pump cycle architectures and the effective utilization of waste heat are becoming more important.
This study presents the development of a cascaded high-temperature heat pump using R-717 (ammonia) as refrigerant in the low-temperature stage and R-601 (pentane) in the high-temperature stage, with the intention of providing heat above 160 °C with a temperature lift of up to 170 K. The architecture incorporates a three-stage compression cycle with oil-injected screw compressors. The system is investigated using a numerical model. The various components were modelled based on the manufacturer's specifications and then validated using corresponding measurement data. The study examines the effects of integrating waste heat from industrial processes at a temperature level above the regular heat source temperature as well as the opportunities and challenges arising from the use of oil-cooled screw compressors.

Selection and/or peer-review under the responsibility of the organizers of the 15th IEA Heat Pump Conference 2026.

Keywords: High-temperature heat pump; System simulation; Modelica; Waste heat utilization;

1. Introduction

High-temperature heat pumps (HTHPs) are a key option to electrify and decarbonize industrial process heat by upgrading available waste heat to supply temperatures well above 100 °C, thereby displacing fossil-fired steam and thermal-oil systems. Despite rapid progress, large-scale industrial deployment remains constrained by techno-economic and practical barriers documented in recent IEA activities: installation cost and system complexity relative to boilers, limited availability of components capable of high temperature lifts—most notably compressors and suitable working fluids—and the need for better standardization and comparable performance data at elevated temperatures. Moreover, high performance hinges on an application-specific match between heat-source and heat-sink profiles; selecting an appropriate system architecture and refrigerant for a given process is non-trivial, and multiple cycle solutions are needed across the broad range of industrial temperature requirements. [1]

Model-based development has therefore become a central element of current practice. Prior work has shown the value of physics-based models assembled in Dymola [2][3][4] with component libraries such as TIL [5] to integrate manufacturer data, generate consistent operating points, and prepare test campaigns more efficiently and safely helping to focus laboratory effort and reduce the risk of critical conditions or infeasible operating regions being only discovered during commissioning. While several studies employ dynamic models for validation under varying conditions, the same modelling ecosystem is widely used to build component-conform system models and to support design and control concept definition before testing.

Against this background, the present paper reports the design and steady-state modelling of a cascaded high-temperature heat pump that combines a low-temperature stage using ammonia (R-717) as working fluid with a high-temperature stage using n-pentane (R-601). The system target is to supply hot-water outlet temperatures between 140 °C and 170 °C from heat-source inlet temperatures between 5 °C and 45 °C, while providing heating capacities between approximately 500 kW and 2000 kW to the water being heated. The model is built from component models that describe manufacturer specifications—including oil-injected screw compressors—in Modelica/Dymola with the TIL suite to generate feasible stationary operating points across the intended operating map and to support the associated control concept for commissioning. Consistent with the integration guidance highlighted in the literature [6] [7], the study also considers the use of waste heat that is occasionally available at elevated source temperatures; when properly matched to the sink requirements within the presented cascade architecture, such integration can raise efficiency even if the higher-temperature source cannot continuously cover the baseload.

Finally, the implications of employing oil-injected screw compressors are addressed explicitly. Large oil flows are required for sealing, lubrication, and cooling [8]; the resulting heat is removed sensibly via the oil circuit and must be handled in the overall heat-recovery concept. These compressor- and oil-circuit specifics—common in MW-scale ammonia systems—are reflected in the component descriptions used here and inform the steady-state operating-point generation that precedes experimental work.

2. Methods

2.1. Description of the developed high temperature heat pump

The high-temperature heat pump is a cascade system consisting of a two-stage ammonia (R-717) cycle with saturated intermediate-pressure suction and a single-stage pentane (R-601) cycle configured as a standard vapor-compression cycle with an internal heat exchanger. Figure 1 illustrates the cascade architecture including the control strategy. The three main heat exchangers, the R-717 evaporator (HX1), the cascade heat exchanger (HX2), and the R-601 condenser (HX3), are plate-and-shell units.

The low-pressure R-717 screw compressor (C1) is speed-controlled and features a variable built-in volume ratio (Vi) to efficiently accommodate varying source-side conditions and to avoid over- and under-compression. In addition, a slide-valve control allows the flow rate to be reduced below the minimum speed; however, when selecting the compressors, the design aimed to avoid this operating mode, as slide-valve control is less efficient than speed control [8]. The high-pressure R-717 compressor (C2) is also speed-controlled; however, due to its special high-pressure design, it features a fixed Vi of 1.8. Over- and under-compression are prevented here by maintaining fixed R-717 mid- and high-pressure setpoints. The R-601 compressor (C3) likewise has a variable Vi to respond optimally to variable sink-side conditions and is speed-controlled.

R-717 stage control:

- The intermediate pressure level is regulated to a pressure of 30 bar by the compressor C1.
- The compressor C2 controls the subcooling of R-717 downstream of the cascade heat exchanger (HX2).
- Expansion valve V2 controls the R-717 high pressure to approximately 56 bar ($\vartheta_{sat} = 95\ °C$)
- Expansion valve V1 regulates the liquid level in the R-717 evaporator (HX1).

R-601 stage control:

- The compressor C3 controls the required heating-water supply temperature.
- The expansion valve V3 controls the R-601 liquid level in the cascade heat exchanger (HX2).

All three screw compressors are oil-injected. As noted, the oil serves three primary functions: sealing, lubrication, and cooling of the working fluid and the screw rotors [8]. For the R-717 compressors, the oil flow is adjusted such that the discharge temperature limits of 90 °C (C1) and 120 °C (C2) are not exceeded. In addition, the oil return temperature to the compressor is controlled to ensure sufficient viscosity and thus reliable lubrication. Owing to the high isentropic exponent of ammonia, the required oil-cooling duty is so large that, across all operating points, the required oil flow rates remain within their allowable bounds. For the R-601 compressor, by contrast, it must be ensured that the unit is sufficiently supplied with oil; controlling to a fixed discharge temperature would, in some operating points, remove too much heat from the R-601 and could lead to compression in the two-phase region and therefore to problems with the oil separation.

The process is depicted in the lg(p)–h diagram for a representative operating point in Figure 2 for the R-717 cycle and in Figure 3 for the R-601 cycle.

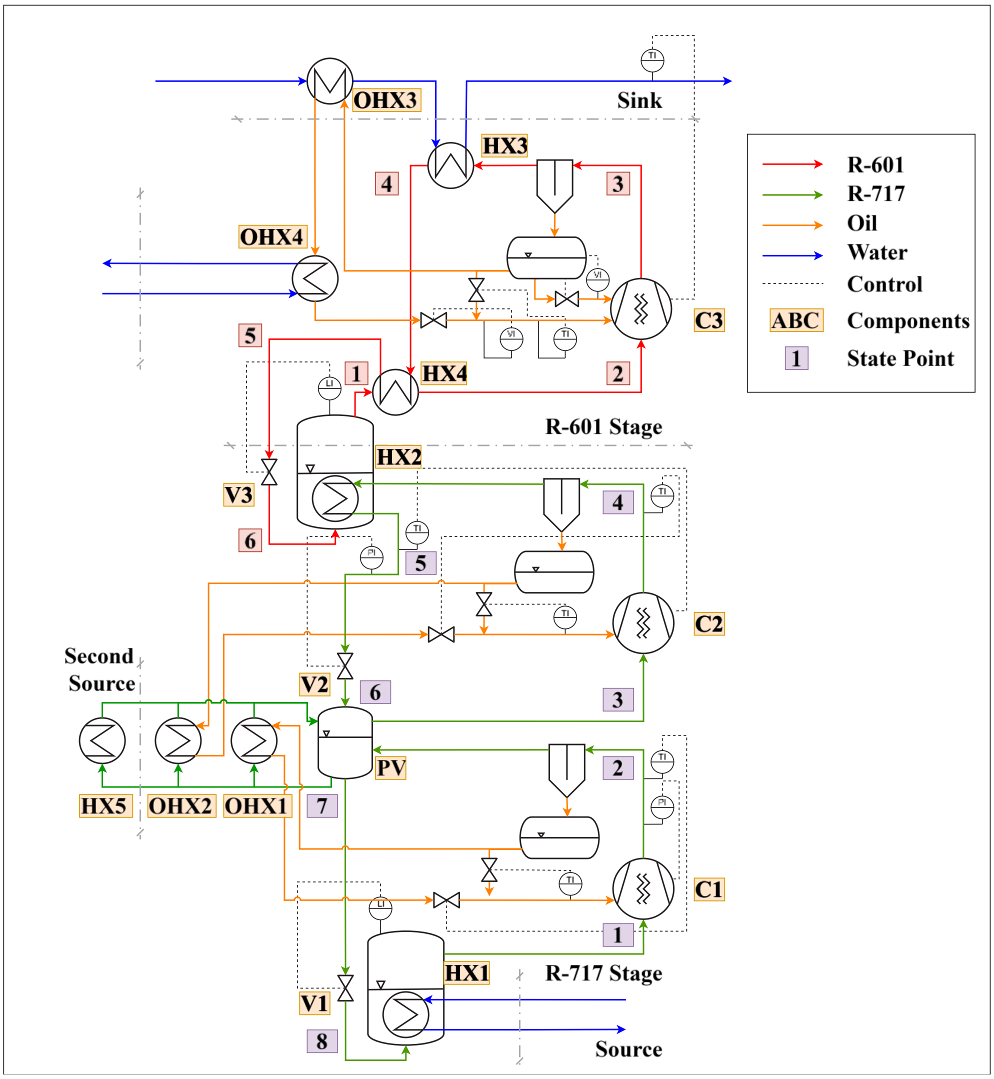

Figure 1. Schematic of the cascaded R-717 / R-601 high-temperature heat pump and control concept.

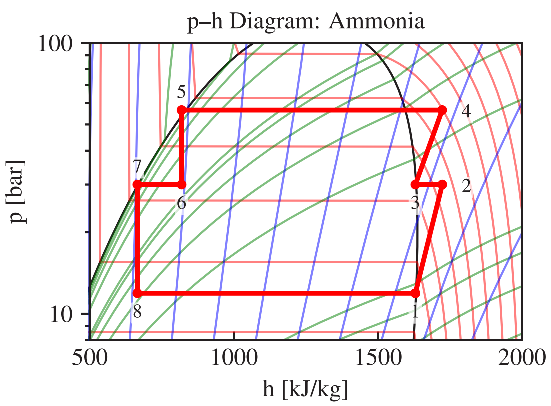

Figure 2. Lg(p)–h diagram of the R-717 (ammonia) low-temperature cycle.

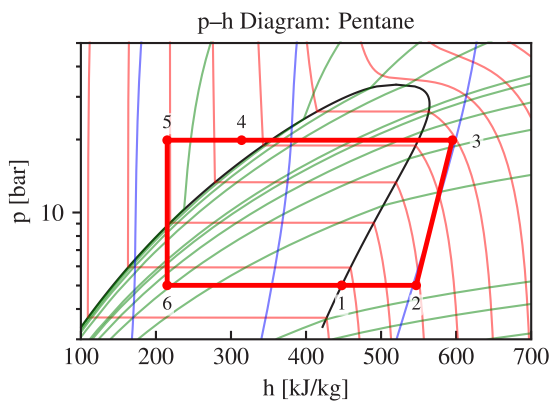

Figure 3 Lg(p)–h diagram of the R-601 (pentane) high-temperature cycle.

2.2. Waste-heat integration

In industrial processes, waste heat is often available at a temperature level that cannot be directly utilized but is well suited to serve as a heat source for heat pumps. To use such waste heat exergetically efficiently at higher temperature levels, it must be integrated appropriately and employed in a way that increases the efficiency of the vapor-compression cycle.

In the system investigated here, the intermediate pressure vessel (PV) in the R-717 cycle, operating at pressure of 30 bar ($\vartheta_{sat} \approx 65$ °C), is designed to enable the evaporation of R-717 using waste heat that is available at a higher temperature level via an additional heat exchanger (HX5). This configuration allows the compressor C1 to be partially relieved, as part of the vapor generation on the intermediate pressure level is provided externally by the recovered waste heat.

The heat removed from the working fluid during compression through oil injection is stored in the oil. Since this heat is sensible rather than latent (as with condensing refrigerant), it is more challenging to reintegrate the oil heat effectively into the process, particularly because the oil must be returned to the compressor at a sufficiently low temperature to maintain adequate viscosity and lubrication. In the present cycle architecture, the oil heat from both R-717 compressors can be used to evaporate liquid R-717 in the intermediate pressure vessel (PV), thereby providing a useful contribution to the process. It must be ensured that the oil inlet temperatures of the compressors remain higher than the evaporation temperature of R-717 at the intermediate pressure ($\vartheta_{sat} \approx 65\,°C$), which is the case in this setup.

The oil heat of the R-601 compressor, however, is only partially recoverable on the sink side, depending on the boundary conditions. A specific feature of the R-601 compressor is that only part of the recirculated oil is cooled, while the remaining fraction is returned to the compressor at discharge temperature to avoid excessive heat removal and prevent condensation of the R-601 within the compression process. The cooled fraction is first transferred to the sink side via OHX3, where it delivers useful heat to the heating water. It is then further cooled in an additional heat exchanger (OHX4) to the required return temperature. In this study, the heat released in OHX4 is initially considered non-usable, although it could potentially be recovered elsewhere in an integrated process.

2.3. Modeling and Simulation Approach

The dynamic model of the high-temperature heat pump was developed in Dymola [2] using components from the TIL library [5], which is based on the modelling language Modelica [9]. The overall modelling approach follows the methodology presented by Kramer et al. [10].

In the first step, the required components were modeled and parametrized based on manufacturer data. The main customized and newly developed components are the plate-and-shell heat exchangers and a modularized compressor model, both of which are described in the following sections. These components were derived from existing elements of the TIL library [5] and were extended and adapted within the given framework. Each component was then fitted to reference data. For this purpose, the individual component models were exported as Functional Mock-up Units (FMUs) [11] and calibrated using Python with the Levenberg–Marquardt algorithm from the SciPy package [12].

In the second step, the developed components were integrated into a complete system model of the heat pump cycle. A dedicated control strategy was implemented, and all relevant PI controllers were tuned accordingly.

In the final step, the complete system model was exported as an FMU to perform parameter studies. These studies were executed and analyzed using a Python script, which automatically varied the boundary conditions listed in Table 1 and performed a simulation for each parameter combination. The dynamic model of the HTHP, together with its control concept, had to reach a steady-state operating point for every simulated case.

Table 1. Parameters varied for parameter study

Parameter	Unit	Range	Step size
Source inlet water temperature	°C	5 … 45	20
Sink mass flow	kg/s	5 … 14	1
Sink water target temperature	°C	140 … 170	10
Sink water temperature lift	K	20 … 40	10

Three distinct configurations were investigated:

- Case 1: Full simulation model as shown in the P&ID in Figure 1.
- Case 2: Oil-circuit heat from the R-717 compressors (C1 and C2) was not recovered in intermediate pressure vessel (PV) and was treated as non-usable.
- Case 3: Identical to Case 1, but with an additional 100 kW of waste heat integrated via the additional heat exchanger HX5, representing higher-temperature waste-heat integration.

For all three cases, a parameter study was performed using the combinations of input variables summarized in Table 1. The results of these studies are presented and discussed in the chapter 3.

For all valid steady-state points, the coefficient of performance (COP) and the temperature lift ΔT_{lift} were determined as key performance indicators according to Eqs. (1) and (2):

$$COP = \frac{\dot{Q}_{Sink}}{P_{C1}+P_{C2}+P_{C3}} \;\; with \;\; \dot{Q}_{Sink} = \dot{Q}_{HX3} + \dot{Q}_{OHX3} \tag{1}$$

$$\Delta T_{lift} = \vartheta_{C,R601} - \vartheta_{0,R717} \tag{2}$$

where $\dot{Q}_{Sink}$ is the total useful heat supplied to the sink, including the contribution from the oil heat exchanger OHX3. The compressor power inputs P_{C1}, P_{C2} and P_{C3} represent the shaft power consumption of the three screw compressors.

In addition, the second-law efficiency η_{Carnot} was calculated to evaluate the thermodynamic quality of the cycle:

$$\eta_{Carnot} = \frac{COP}{COP_{Carnot}} \;\; with \;\; COP_{Carnot} = \frac{T_{C,R601}}{T_{C,R601}-T_{0,R717}} \tag{3}$$

2.3.1. Screw compressor model

The developed screw compressor model is based on a 20-coefficient polynomial approach [13], which depends on the evaporation temperature (ϑ_0), condensation temperature (ϑ_C), rotational speed (n), and 20 fitted coefficients ($k_1 \dots k_{20}$). Using this formulation, both the mass flow rate and the power consumption of the compressor can be calculated according to Eq. (4):

$$P, \dot{m} = f(\vartheta_0, \vartheta_C, n, k_1 \dots k_{20}) \tag{4}$$

The 20 coefficients were identified for each of the three screw compressors, separately for mass flow rate and power consumption, based on manufacturer reference data. For this purpose, data points were extracted from a large portion of each compressor's performance map, covering various rotational speeds as well as evaporation and condensation temperatures. The datasets were sampled quasi-equidistantly across the relevant operating range to ensure balanced coverage of the parameter space.

Figure 4 shows as an example the fitting results for the screw compressor C2, illustrating the relative deviation of the predicted power and mass flow with respect to the corresponding reference values. The color scale indicates the pressure ratio (π). A total of 624 reference points were used for this compressor, resulting in a mean absolute relative error (MARE) of 0.9 % for the mass flow rate and 1.1 % for the power consumption. The results for the other compressors are of comparable accuracy.

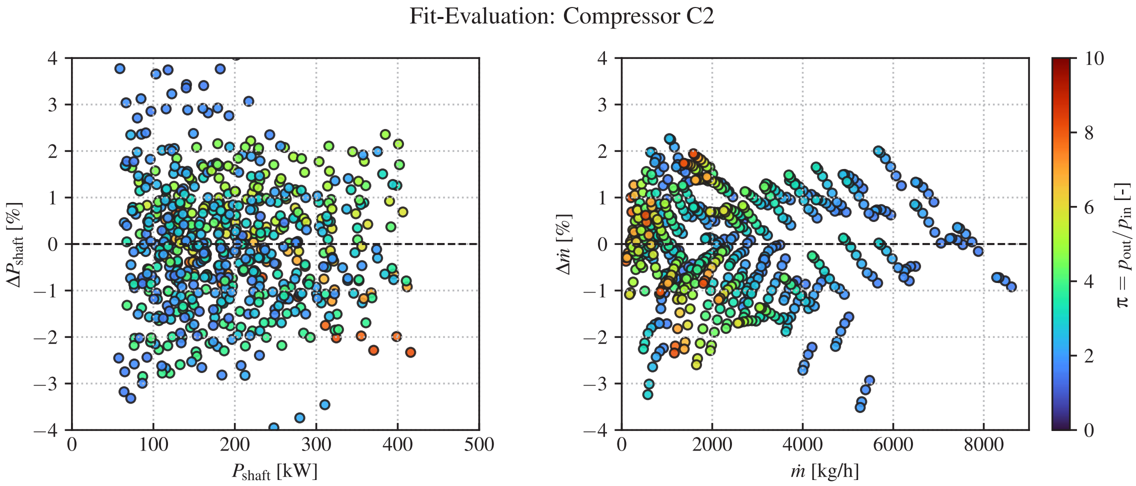

Figure 4. Relative deviation between fitted and reference data for the R-717 high-pressure screw compressor.

The compressor model also accounts for cooling by oil injection. It is assumed that at the compressor outlet, the oil (indexed with "oil") and the refrigerant (indexed with "ref") leave the compressor at the same temperature, as expressed in Eq. (5):

$$\vartheta_{oil,out} = \vartheta_{dis,cooled} \tag{5}$$

The heat removed by the oil can then be calculated according to Eq. (6). It is determined from the refrigerant mass flow rate ($\dot{m}_{ref}$) and the difference between the hypothetical discharge enthalpy h_{dis^*} (without oil cooling) and the actual discharge enthalpy h_{dis} (with cooling):

$$\dot{Q}_{oil} = \dot{m}_{ref} \cdot \left(h_{dis^*} - h_{dis}(\vartheta_{dis}, p_C)\right) \tag{6}$$

The uncooled enthalpy (h_{dis^*}) is determined from the isentropic relationship in combination with the power consumption calculated by the 20-coefficient polynomial. Together, Eqs. (6) and (7) form a solvable system of equations, where Eq. (7) represents the heat absorbed by the oil:

$$\dot{Q}_{oil} = \dot{m}_{oil} \cdot c_{p,oil} \cdot (\vartheta_{oil,out} - \vartheta_{oil,in}) \tag{7}$$

This approach results in a robust and computationally efficient compressor model that can be readily integrated into system-level simulations of the heat pump.

2.3.2. Heat exchanger model

The Heat exchangers HX1, HX2 and HX3 in the model are of the plate-and-shell type. Owing to the modular structure of the TIL library, a corresponding representation of this geometry could be implemented. TIL allows the discretization of heat exchangers into an arbitrary number of computational cells; in this work, five cells were selected for all units as a compromise between computational efficiency and spatial resolution.

Each heat exchanger was parametrized using manufacturer data to ensure that geometric properties such as heat-transfer area, wall thickness, and internal volume match the real components. For the refrigerant side, the Longo correlations [14], [15], [16] were applied for both evaporation and condensation processes. On the water side, correlations according to [17] were used.

Similar to the compressor models, the heat exchanger models were validated against measurement data, and selected parameters were adjusted accordingly. A constant correction factor f_{corr} was applied to the calculated heat-transfer coefficient α for each heat-transfer regime (single-phase, condensation, evaporation).

For model validation, experimental data from a wide range of evaporators and condensers operating with ammonia and water were used. The comparison between simulated and measured heat duties is shown exemplarily in Figure 5 for HX1. The results cover a capacity range from approximately 200 kW to nearly 2

MW, and by fitting a limited number of parameters, the model achieved good agreement with the measurement data.

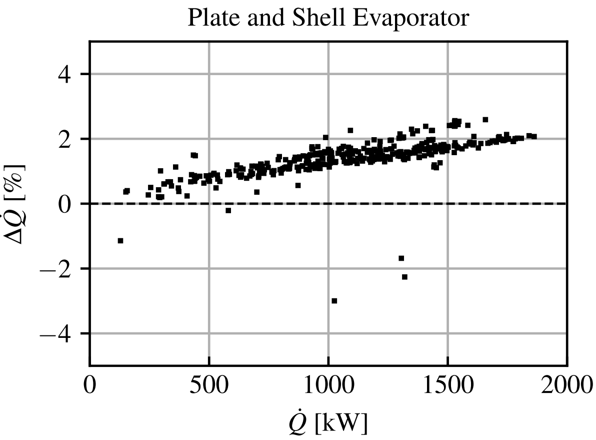

Figure 5. Comparison of simulated and measured heat duties for the evaporator model.

3. Results and Discussions

Before evaluating the simulation results, all operating points were carefully filtered to ensure physically meaningful and comparable data. Only those points were considered where (i) the target sink outlet temperature was reached, (ii) the intermediate pressure in the R-717 stage remained close to its setpoint of 30 bar (since the compressor C2 has a fixed built-in volume ratio), (iii) the discharge temperature of the compressor C3 exceeded the condensation temperature of R-601 by at least 10 K. This last criterion ensured that the compressor operated safely outside the wet-vapor region. (iv) In addition, only simulations that reached a steady-state operating condition were retained for the subsequent analysis.

It should be noted that the PI controllers of the overall system were tuned for a limited range of operating points. As a result, certain simulated conditions failed to converge or even caused the solver to abort. These non-stationary runs were also excluded from the dataset.

Figure 6 presents all valid results of the parameter study, showing the coefficient of performance (COP) as a function of the temperature lift ΔT_{lift} for the three investigated source inlet temperatures of 45 °C, 25 °C, and 5 °C.

Dashed regression lines are added as visual aids to illustrate the general trend of the data.

Across all three cases and source temperatures, a consistent qualitative behaviour can be observed: the COP decreases with increasing temperature lift. The investigated range extends approximately from 100 K to 170 K. The ranking of the three cases remains unchanged throughout this range - Case 3 has the highest COP, Case 1 serves as the reference, and Case 2 (without utilization of the oil-cooler heat from OHX1 & OHX2) consistently performs worst. Furthermore, a comparison among the three source temperatures reveals that, as expected, the COP decreases with decreasing source inlet temperature due to the corresponding increase in temperature lift.

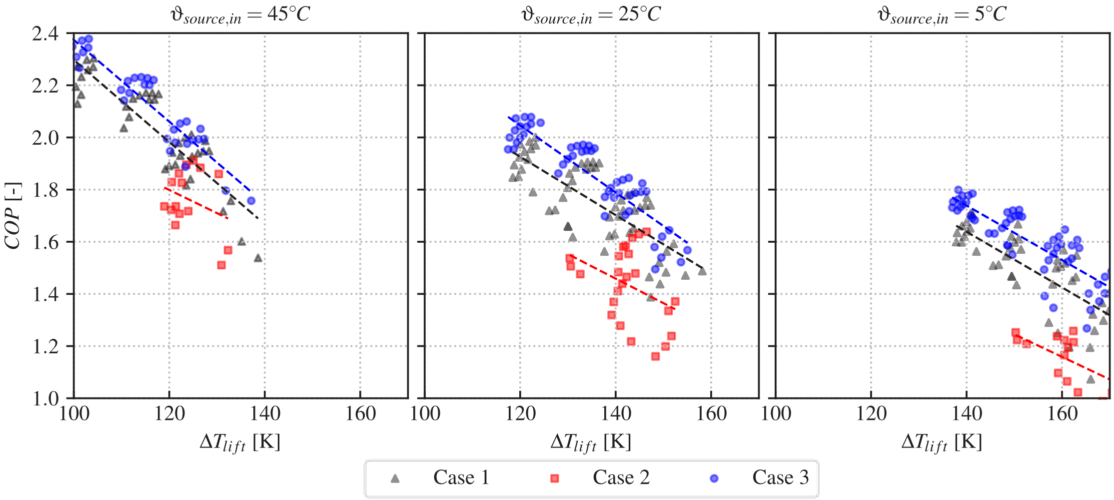

Figure 6. COP as a function of temperature lift for three source temperatures and three operating cases.

The superior performance of Cases 1 and 3 is directly related to the integration of oil-circuit waste heat from the R-717 compressors (OHX1/2). This heat is transferred to the intermediate pressure vessel, where the liquid R-717 is evaporated at 30 bar. As a consequence, the R-717 low-pressure stage is partially relieved, and the compressor C1 can operate at a lower rotational speed and therefore with reduced shaft power input, resulting in an overall higher COP. In Case 3, the effect is further amplified by the injection of an additional 100 kW of process waste heat into the mid-pressure separator via heat exchanger HX5.

According to the fitted trend lines, this additional thermal input yields a nearly constant COP increase of about 5 % compared with Case 1 across the entire range of temperature lifts, under otherwise identical boundary conditions.

In summary, Figure 6 clearly demonstrates the expected dependence of system efficiency on temperature lift and quantifies the positive impact of integrating oil-circuit and process waste heat at the intermediate pressure level in the low-temperature stage. Neglecting this integration, as in Case 2, leads to a distinct efficiency penalty, whereas Case 3 achieves a robust and consistent performance improvement of roughly 5 % compared to the reference configuration.

In Figure 6, the overall trend of the parameter study was shown, where the coefficient of performance (COP) decreases with increasing temperature lift. This behaviour is thermodynamically expected. However, when examining the individual clusters of data points within each graph, each representing a different target sink outlet temperature, varied in 10 K steps - a different internal trend becomes visible. Within these clusters, the COP does not strictly decrease with increasing temperature lift, but rather shows local variations that suggest additional influencing factors. To explain this behaviour in more detail, Figure 7 provides a closer look at the system performance under controlled boundary conditions.

Figure 7 displays the results of Case 1 only, for a source inlet temperature of 45 °C and a target sink outlet temperature of 160 °C. The three subplots show the COP (left), as a function of the temperature lift ΔT_{lift} (center) the total heating capacity $\dot{Q}_{sink}$, and (right) the mean heat-transfer coefficient of the R-601 in the condenser HX3, $\overline{\alpha}_{HX3,R601}$. The symbols indicate the sink-side temperature spread ($\Delta\vartheta_{sink}$ = 20 K, 30 K, 40 K), while the color scale represents the relative share of non-usable oil-cooler heat from OHX4, defined as $\dot{Q}_{OHX4}\,/(\dot{Q}_{sink} + \dot{Q}_{OHX4})$, which quantifies the fraction of heat not contributing to useful heating output.

Within the data clusters of constant sink outlet temperature, a different local trend can be observed: as the temperature lift ΔT_{lift} increases, the COP also increases for a given sink-side temperature spread $\Delta\vartheta_{sink}$. The temperature lift increases despite the same required target temperature because the water mass flow on the source side remains constant. When the sink-side mass flow (and thus heating capacity $\dot{Q}_{sink}$) increases, the source water is cooled further, leading to a lower R-717 evaporation temperature in HX1 and therefore a larger temperature lift.

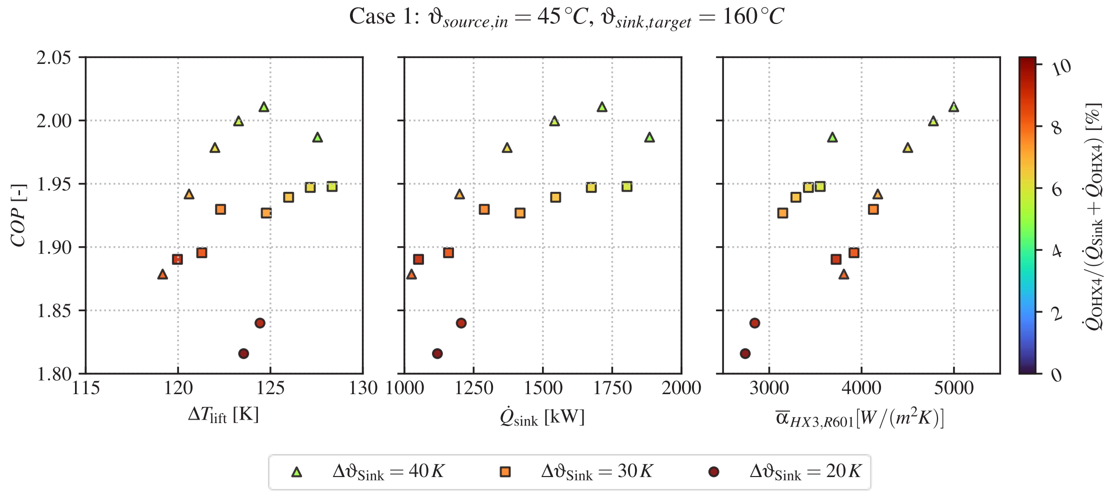

Figure 7. Detailed results for Case 1 (45 °C source, 160 °C sink): COP vs. temperature lift, heating capacity, and mean heat-transfer coefficient.

It can also be clearly seen in Figure 7 that larger temperature spreads on the sink side result in higher COP values. In summary, for a given source inlet temperature and a given sink target temperature the COP increases with increasing heating capacity and decreasing relative oil-heat losses via OHX4 (compare the color bar). The improvement in COP is mainly due to two effects:

- a larger fraction of oil-circuit heat becomes usable for the heating process, and
- higher compressor speeds at greater loads lead to better efficiency, since screw compressors lose efficiency at part-load due to increased internal leakage.

The plots show a small discontinuity for $\Delta\vartheta_{\text{sink}} = 30$ K. This can be explained by the plot on the right-hand side, which shows the mean heat-transfer coefficient, $\overline{\alpha}_{HX3,R601}$. In principle, $\overline{\alpha}_{HX3,R601}$ should increase with rising refrigerant mass flow. However, due to the five-cell discretization of the plate-and-shell heat-exchanger model, one computational cell transitions from two-phase condensation to single-phase liquid cooling (subcooled region) as the load increases. Because the single-phase correlation yields significantly lower heat-transfer coefficients than the condensation correlation, the cell-averaged, $\overline{\alpha}_{HX3,R601}$ drops abruptly—even though both heat load and mass flow increase. This discontinuity is therefore a numerical artifact caused by regime weighting and zone switching within the model.

Overall, the system is capable of reaching sink outlet temperatures of 160 °C at a 45 °C source and provides approximately 1–2 MW of heating capacity.

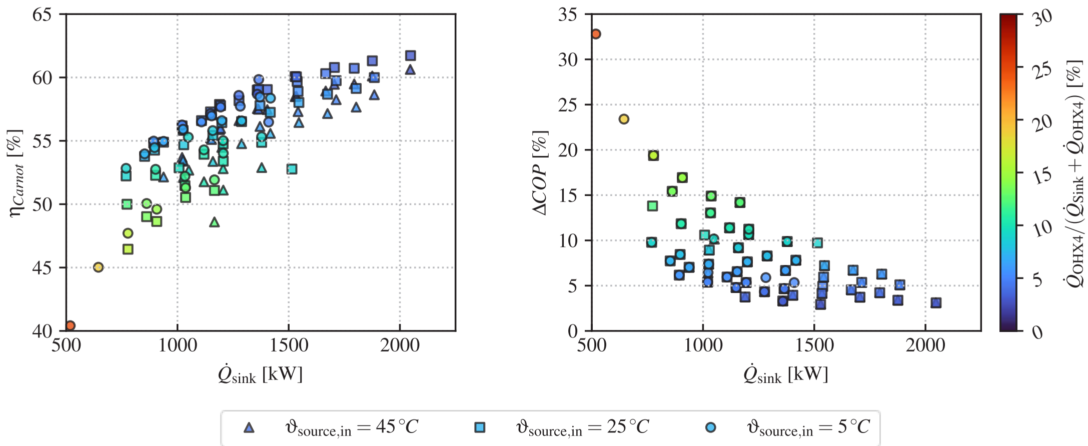

Figure 8. Carnot efficiency and potential COP increase (ΔCOP) as a function of heating capacity for Case 1.

Figure 8 summarizes the overall performance of the system for Case 1. The left-hand plot shows the Carnot efficiency η_{Carnot}, defined as the ratio of the actual COP to the theoretical Carnot COP, plotted against the delivered heating capacity $\dot{Q}_{sink}$. The right-hand plot illustrates the relative change in COP (ΔCOP) that would result if the heat rejected by the oil cooler OHX4 were also considered usable, assuming that this oil heat could be recovered elsewhere in the process. The color scale represents the proportion of total heat occurring in OHX4.

The results confirm that the heat pump achieves Carnot efficiencies between roughly 45 % and 60 %, with some operating points even exceeding 60 %. These values underline the high thermodynamic quality of the cycle concept, especially considering the large temperature lifts of up to 170 K and the oil-injected screw compressors used. If the oil-cooler heat were recovered as assumed for the potential analysis in the right plot, the COP could increase by up to 4–30 % in the selected operating points, depending on the available oil temperature and the effectiveness of the heat integration.

Overall, the results indicate that the investigated configuration performs very well under the given conditions. The assumptions used in the parameter study are deliberately conservative, particularly with respect to the maximum sink-side temperature spread of 40 K. Furthermore, the component design, especially the heat exchangers and compressors, was chosen to cover a wide operating range (from about 500 kW to > 2 MW of heating capacity). This broad design scope leads to non-ideal component efficiencies in parts of the map. In practical applications, however, a heat pump system would typically be optimized for a specific temperature range and load profile. The author therefore expects significantly higher efficiencies for a system tailored to a defined application with appropriately optimized components.

4. Conclusion

The presented study introduced the development and steady-state simulation of a cascaded R-717/R-601 high-temperature heat pump designed for industrial heat supply above 160 °C. The system combines a two-stage R-717 cycle with a single-stage R-601 cycle in cascade design and was modelled in Modelica/Dymola using manufacturer-based compressor and heat-exchanger data. A parameter study was conducted for three configurations to assess the influence of oil-circuit heat recovery and additional waste-heat integration.

The results show that the system performs particularly well at high source temperatures, large sink-side temperature spreads, and high heating capacities. Among the three investigated cases, Case 1 represents the reference configuration with oil-heat recovery from the R-717 compressors, Case 2, without this recovery, exhibited the lowest efficiency, and Case 3, which included an additional 100 kW of higher-temperature waste-heat input at the intermediate pressure level of the R-717 stage, achieved the best performance with an approximate 5 % COP increase over the reference case. Despite the broad design scope of the system, which was not optimized for a single operating point, the achieved efficiencies remain high, reaching 45–60 % of the Carnot limit. This demonstrates that the concept is robust and well suited for varying industrial boundary conditions.

Future work will focus on exergetic analyses and the dynamic behaviour of the plant to better understand transient interactions, control stability, and start-up characteristics. The influence of key boundary conditions, such as required heating capacity, available source temperature, and secondary-side temperature spread, will be analysed in more detail, as these factors strongly affect both efficiency and economic feasibility. Furthermore, the control system will be improved to ensure stable operation and a higher number of converging steady-state points under varying conditions. To enhance model accuracy, the heat exchangers will be discretized more finely, accepting higher computational effort in exchange for improved spatial resolution and predictive quality.

Overall, the study confirms the technical feasibility and strong performance potential of cascaded high-temperature heat pumps with integrated waste-heat utilization and highlights the importance of component optimization and control refinement for future system designs.

References

[1] B. Zühlsdorf, 'Annex 58 – Task 1: Technologies Task Report', 2024. [Online]. Available: https://heatpumpingtechnologies.org/project58/task-5-dissemination/

[2] 'Dymola', Dassault Systèmes. Accessed: Nov. 09, 2025. [Online]. Available: https://www.3ds.com/de/products/catia/dymola

[3] W. Meesenburg, Kofler, and Ommen, 'Design considerations for dynamically operated large-scale ammonia heat pumps.' International Institute of Refrigeration (IIR). doi: 10.18462/IIR.ICR.2019.1203.

[4] 'Digital twins for large-scale heat pumps and refrigeration systems'. Accessed: Nov. 15, 2025. [Online]. Available: https://www.dti.dk/projects/digital-twins/41553

[5] S. User, 'TLK-Thermo GmbH'. Feb. 27, 2022. Accessed: Feb. 27, 2022. [Online]. Available: https://www.tlk-thermo.com

[6] B. Zühlsdorf, 'Annex 58 – Task 2 Integration Concepts Report', 2024. [Online]. Available: https://heatpumpingtechnologies.org/project58/task-5-dissemination/

[7] M. P. Andersen, 'High-Temperature Heat Pumps - Integration, Design, and Cycle Selection for Industrial Applications', DTU, Department of Civil and Mechanical Engineering.

[8] L. Rinder, *Schraubenverdichter*. Wien New York: Springer, 1979.

[9] 'Modelica'. Accessed: Nov. 09, 2025. [Online]. Available: https://modelica.org/

[10] K. R. Kramer, J. L. Poulsen, W. Meesenburg, and M. Kj, 'Analysis of Large-Scale Ammonia Heat Pumps in Transient Operating Conditions', 2023.

[11] 'Functional Mock-up Interface'. Accessed: Nov. 09, 2025. [Online]. Available: https://fmi-standard.org/

[12] P. Virtanen *et al.*, 'SciPy 1.0: fundamental algorithms for scientific computing in Python', *Nat. Methods*, vol. 17, no. 3, pp. 261–272, Mar. 2020, doi: 10.1038/s41592-019-0686-2.

[13] R. Ossorio and E. Navarro-Peris, 'Testing of Variable-Speed Scroll Compressors and their inverters for the evaluation of compact energy consumption models', *Appl. Therm. Eng.*, vol. 230, p. 120725, July 2023, doi: 10.1016/j.applthermaleng.2023.120725.

[14] G. A. Longo, 'Hydrocarbon Refrigerant Vaporization Inside a Brazed Plate Heat Exchanger', *J. Heat Transf.*, vol. 134, no. 10, Art. no. 10, Oct. 2012, doi: 10.1115/1.4006817.

[15] G. A. Longo, G. Righetti, and C. Zilio, 'A new computational procedure for refrigerant condensation inside herringbone-type Brazed Plate Heat Exchangers', *Int. J. Heat Mass Transf.*, vol. 82, pp. 530–536, Mar. 2015, doi: 10.1016/j.ijheatmasstransfer.2014.11.032.

[16] G. A. Longo and A. Gasparella, 'Heat transfer and pressure drop during HFC refrigerant vaporisation inside a brazed plate heat exchanger', *Int. J. Heat Mass Transf.*, vol. 50, no. 25–26, Art. no. 25–26, Dec. 2007, doi: 10.1016/j.ijheatmasstransfer.2007.07.001.

[17] VDI e. V., Ed., *VDI-Wärmeatlas*. Berlin, Heidelberg: Springer Berlin Heidelberg, 2013. doi: 10.1007/978-3-642-19981-3.